

Improving Potential Energy Surfaces Using Experimental Feshbach Resonance Tomography

Karl P. Horn,^{1†} Luis Itza Vazquez-Salazar,^{2†}
Christiane P. Koch¹ & Markus Meuwly^{2*}

¹Dahlem Center for Complex Quantum Systems and Fachbereich Physik,
Freie Universität Berlin, Arnimallee 14, D-14195 Berlin, Germany

²Department of Chemistry, University of Basel,
Klingelbergstrasse 80 , CH-4056 Basel, Switzerland.

† These authors contributed equally

*To whom correspondence should be addressed; E-mail: m.meuwly@unibas.ch

Supplementary materials

Materials and Methods

Supplementary Text

Figs. S1 to S32

Table S1

S1 The Optimization procedure

To obtain the morphing parameters (α , β and ε), the NLOpt suite (41) was used. Given the optimisation space's complexity, the subplex algorithm (42) implemented in NLOpt, which does not require derivatives, was used for the procedure. In the subplex algorithm, the method breaks the parameter search into a sequence of subspaces. In each subspace, the algorithm uses the Nelder-Mead algorithm to optimize the loss function. The subplex algorithm is more efficient and robust than the original Nelder-Mead (43).

The results obtained from using NLOpt depend on the initialization of the parameters. For this work, we initialize all parameters to 1 which yields the unmodified PES. To avoid unphysical results, the algorithm is constrained to a lower bound such as $\mathbb{R}^+ > 0$ for α and β parameters, therefore constrained to 0.01. The value ε that controls the energy was left unconstrained for the lower bound. The upper bound of α was constrained to a maximum value of 1.1 because any value larger than that would imply dissociation of the H_2^+ molecule. For the other parameters (β and ε), the upper bound was set to 10.

S2 (Global) angular power morphing of MP2

In addition to morphing distances and the energy scale, angular morphing was explored. Including the angular degree of freedom in morphing the PES is less straight forward, since any morphing transformation should conserve the underlying symmetry of the PES. Thus, straight-forward linear scaling of the angle θ in the present case is not possible. Instead, the transformation needs to leave $\theta = 0, \pi/2$ (since the dihydrogen ion is homonuclear) and π invariant. One

possible transformation which fulfills this requirement is

$$f_\eta(\theta) = \pi \left(1 - H\left(\frac{\theta}{\pi} - \frac{1}{2}\right) \right) \frac{1}{2} \left(\frac{2\theta}{\pi} \right)^\eta + \pi \cdot H\left(\frac{\theta}{\pi} - \frac{1}{2}\right) \left(1 - \frac{1}{2} \left(2 - \frac{2\theta}{\pi} \right)^\eta \right). \quad (\text{S1})$$

Here, $H(x)$ is the Heaviside step function defined as:

$$H(x) = \begin{cases} 0 & \text{If } x < 0 \\ 0.5 & \text{If } x = 0 \\ 1 & \text{If } x > 0 \end{cases} \quad (\text{S2})$$

The first term in equation S1 is responsible for morphing angles $\theta < \pi/2$, whereas the second term is the mirror image around the $(\pi/2, \pi/2)$ point, responsible for morphing angles $\theta > \pi/2$ and $f_\eta(\pi/2) = \pi/2$ (See Figure S32).

The effect of including the angular coordinate in the morphing was explored by morphing the MP2 PES to the FCI PES as described in the main manuscript. The optimization procedure reduces the RMSE between FCI and the morphed PES by around 40 % from (138 cm^{-1} to 75 cm^{-1}). This compares with an improvement by 30 % (138 cm^{-1} to 87 cm^{-1}) without morphing the angle. Figure S19 shows the ensuing changes in the PES. The result of including angular morphing for M2 applied to the MP2 PES is shown in Figs S20 and S21. It is found that the total loss improves by a factor of two compared to morphing without the angular degree of freedom and for the PES-to-PES morphing the RMSE improves by 25 % (Figure S17).

S3 Two-body potential fitting

In this work, the two-body interaction energy for a molecule AB was expressed as (19, 44, 45)

$$\mathcal{V}_{AB}^{(2)}(R_{AB}) = \frac{c_0 e^{-\alpha_{AB} R_{AB}}}{R_{AB}} + \sum_{i=1}^M C_i \rho_{AB}^i + \mathcal{V}_{long}(\tilde{r}) \quad (\text{S3})$$

In equation S3, C_i are linear coefficients with $C_0 > 0$ to assure that the diatomic potential remains repulsive ($V_{AB}(r_{AB}) \rightarrow \infty$) for $r_{AB} \rightarrow 0$ and ρ_{AB}^i is defined as:

$$\rho_{AB}^i = R_{AB} e^{-\beta_{AB}^{(2)} R_{AB}} \quad (\text{S4})$$

The long range part of equation S3 is written as (46):

$$\mathcal{V}_{long}(\tilde{r}) = -\frac{\alpha_d q^2}{2\tilde{r}^4} - \frac{\alpha_q q^2}{2\tilde{r}^6} - \frac{\alpha_o q^2}{2\tilde{r}^8} - \frac{\beta_{ddq} q^3}{6\tilde{r}^7} - \frac{\gamma_d q^4}{24\tilde{r}^8} \quad (\text{S5})$$

In equation S5, q is the charge, α_i , $i \in \{d, q, o\}$ are the dipole, quadrupole and octupole polarizabilities for H and He atoms, respectively, and β_{ddq} and γ_d are the first and second hyperpolarizabilities, respectively. Values for these parameters were taken from Refs. 46, 47. Finally, the coordinate \tilde{r} , whose objective is to remove the divergence of the long-range terms at short separations of H-H and H-He, is defined as (48)

$$\tilde{r} = r + r_l \exp(-(r - r_e)) \quad (\text{S6})$$

Here, r_l is a distance parameter, and r_e is the equilibrium bond distance of the diatomic molecule. The linear coefficients C_i and the parameters α_{AB} and $\beta_{AB}^{(2)}$ in equations S5 and S4 were taken from Ref. 19 for FCI and MRCI potentials. For the MP2 potential, the values were determined using the same method as described in Ref. 19 and are given in Table S1.

Coefficients	H_2^+	HeH^+
C_0	1.01921689	10.7720718
α	1.64361518	2.37373920
C_1	-0.73449753	-4.46348296
C_2	5.10324938	59.1487168
C_3	-81.5643228	-3857.67751
C_4	847.329344	104277.881
C_5	-5377.78872	-1890643.12
C_6	21730.0685	21015000.8
C_7	-56454.3034	-1.3583E+08
C_8	91470.4779	4.1364E+08
C_9	-84131.3637	-29244093.5
C_{10}	33516.3571	-2.0736E+09
β	0.99789130	2.23414441

Table S1: Coefficients for the MP2/aug-cc-pV5Z diatomic potentials.

S4 Morphing M1 for the MRCI and MP2 PESs

Multi-Reference CI: Figure 2B compares the cross sections from experiments with the results from computations with PESs before and after morphing M1 for the MRCI+Q PES. Overall, the RMSE for the energies changes from 10.3 to 12.2 cm⁻¹, whereas the intensities improve from an RMSE of 23.9 to 21.9 arb. u. The results indicate that M1 has the most pronounced impact on intermediate values of j' (i.e. $j' = 4, 5$); see Figures 2D and E. Changes in the peak energies do not show a clear trend. The largest improvements are observed for $j' = 5$ and for $j' = [0, 1]$. Errors for peaks with $j' = 8$ and $j' = 6$ do not reduce using M1. The remaining peaks showed an increase in the error after applying M1. For the peak intensity, again, the largest improvement is observed for the $j' = [0, 1]$ peak. For most other peaks, with the exception of $j' = 5$ and $j' = 8$, there is clearly an improvement in the intensities.

The initial and morphed MRCI PESs are compared in Figure 3B. In this case, morphing increases the anisotropy at long-range compared to the initial PES. However, changes are more pronounced than for the FCI PES. One-dimensional cuts along the r_{HH} and R coordinates for given angle θ are provided in Figures S25 and S26. As for the FCI PES, the difference between the initial surface and the morphed surface are more pronounced as r_{HH} increases. The 1D cuts of the surface at different values of r_{HH} (Figure S26) show further evidence of the change in the depth of the potential well. The modifications of the energy curves with respect to the r_{HH} coordinate follow the same trend as the FCI surface.

MP2: The results for the lowest-quality surface (MP2) are shown in Figures 2C and 3C. The RMSE for the energies improves from 13.1 to 12.8 cm⁻¹ whereas for the intensities, it changes from 22.4 to 10.9 arb. u. Particularly notable is the improvement in the intensities by more

than a factor of two. Overall, the changes in the position of the energies and the intensities of the peaks for the calculated cross sections are more pronounced than for the FCI and MRCI+Q PESs. The energy position for peaks with large j' ($j' = 7$ and $j' = 8$) improve by $\approx 5 \text{ cm}^{-1}$. Another difference is that the shoulder of the peak at $j' = 8$ that appears for the two previously described surfaces is not visible for the MP2 surface. For the peaks with $j' = 4$ and $j' = 5$, the error with respect to the experimental spectra upon morphing increases slightly.

The original MP2 PES and its morphed variant for a H_2^+ separation of $r_{\text{HH}} = 2.0 \text{ a}_0$ are reported in Figure 3C. Because Møller-Plesset second-order theory is a single-reference method and makes further approximations, the changes in the topology of the PES are considerably larger than for the FCI and MRCI+Q PESs. Most of the isocontours are compressed compared with the initial MP2 surface, and the well depth is reduced from 2493 cm^{-1} to 1684 cm^{-1} (Table 1), see Figure S27. The one-dimensional cuts along the r_{HH} and R coordinates for given θ , see Figures S28 and S29, show that as r_{HH} increases the single-reference assumption of the method, leading to convergence problems for small R . As a consequence of the contraction of the potential wells, the barrier of the transition state at $\theta \approx 90^\circ$ is increased, which is further confirmed by the Minimum Energy Path (MEP) shown in Figure S30C. A more detailed analysis of the MEP (Figure S31C) reveals a small increase in the energy of the transition state along the angular coordinate θ . On the other hand, for the R -coordinate a non-physical barrier emerges at around 3.5 a_0 .

S5 Resonances under Morphing

The cross sections depending on the binding energy between He and H_2^+ as opposed to the relative kinetic energy of the two reactants shows distinct peaks that are no longer separated by final states (j') of the H_2^+ fragment but rather appear as one or several Feshbach Resonances per input J and ℓ at certain values of the binding energy. Both the energy at which a Feshbach Resonance appears, and the distribution of intensities in all exit channels, depend sensitively on the topography of the PES. In consequence, the effect of morphing on the PES can influence the number, energy and intensities of the Feshbach resonances. To illustrate this, it is instructive to consider projections of wave functions for particular resonances to characterize how changes in the PES, which lead to changes in the collision cross-section, are reflected in the radial and angular behaviour of the wave function.

Figure S8 shows the square of the ($v' = v$) and ($j' = j$) components of the resonance wave functions (first and third rows of panels) and corresponding resonances in the cross-section (second and fourth rows of panels) for the dominant ℓ and J contributions for para- and ortho- H_2^+ for all three unmorphed and morphed PESs, respectively. The number, position(s) and intensities of the spectroscopic features respond to morphing in a largely unpredictable way. As an example, the unmorphed and morphed PESs at the FCI level are considered for para- H_2^+ with ($\ell = 4, J = 4$) (left column, rows 1 and 2 in Figure S8). Although M1 changes the topology of the morphed PES only in a minor fashion, the effect on the wavefunctions and resulting spectroscopic feature is clearly visible. For the unmorphed FCI PES there is one resonance at -8.1 cm^{-1} which splits into two resonances at -2.1 cm^{-1} and -16.3 cm^{-1} of approximately equal height upon morphing the PES. Accordingly, the wavefunctions also differ, in particular in the long-range part, i.e. for large R . Similar observations were made for the wavefunctions on the

MP2 PES, whereas for the MRCI PESs the changes in the wavefunctions are comparatively smaller.

Conversely, for ortho- H_2^+ the resonances of both FCI and MRCI PESs are affected in a comparable fashion and more noticeable changes to the resonance wave function are observed than for para- H_2^+ . Whilst the resonance wave functions are shifted to larger R in the cases of FCI and MP2, the MRCI resonance wave function only experiences a small shift. Significantly, even though the anisotropy of the PESs only changes in a minor fashion under morphing, all three resonance wave functions respond owing to a change in the superposition of outgoing partial wave (quantum number ℓ'). For the FCI and MP2 PESs angular/radial coupling is enhanced by morphing, which leads to elongation of certain lobes in the wavefunctions along the (R, θ) -direction for ortho- H_2^+ -He. This contrasts with para- H_2^+ -He for which unique assignments of the ro-vibrational quantum numbers is possible from conventional node-counting.

S6 Figures

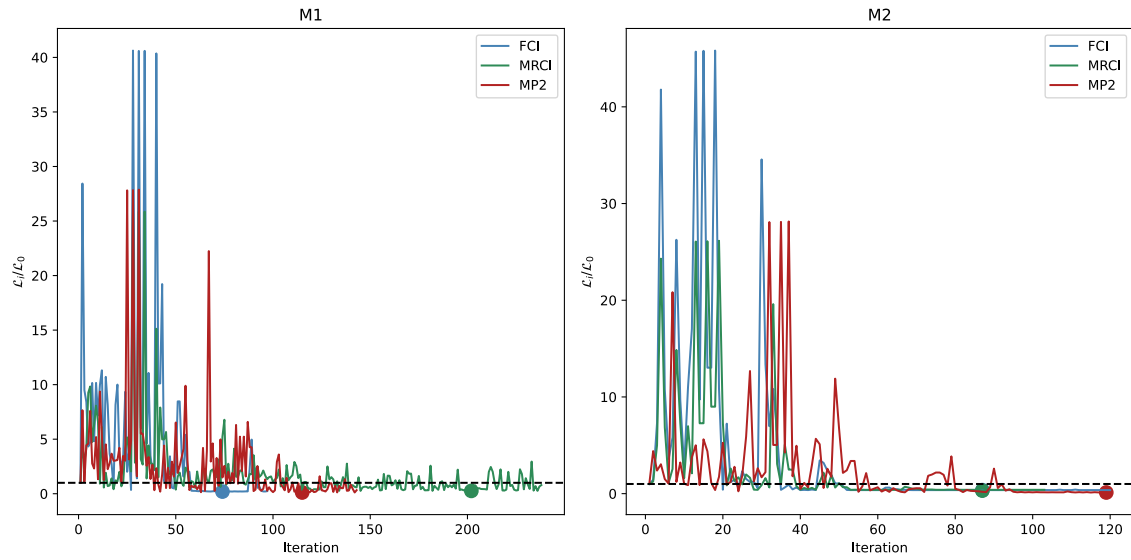


Figure S1: Evolution of the magnitude of the loss (\mathcal{L}_i) over the iterations with respect to the initial value (\mathcal{L}_0) for the M1 (left) and M2 (right) methods. The loss function is defined in Eq. 5 the main manuscript.

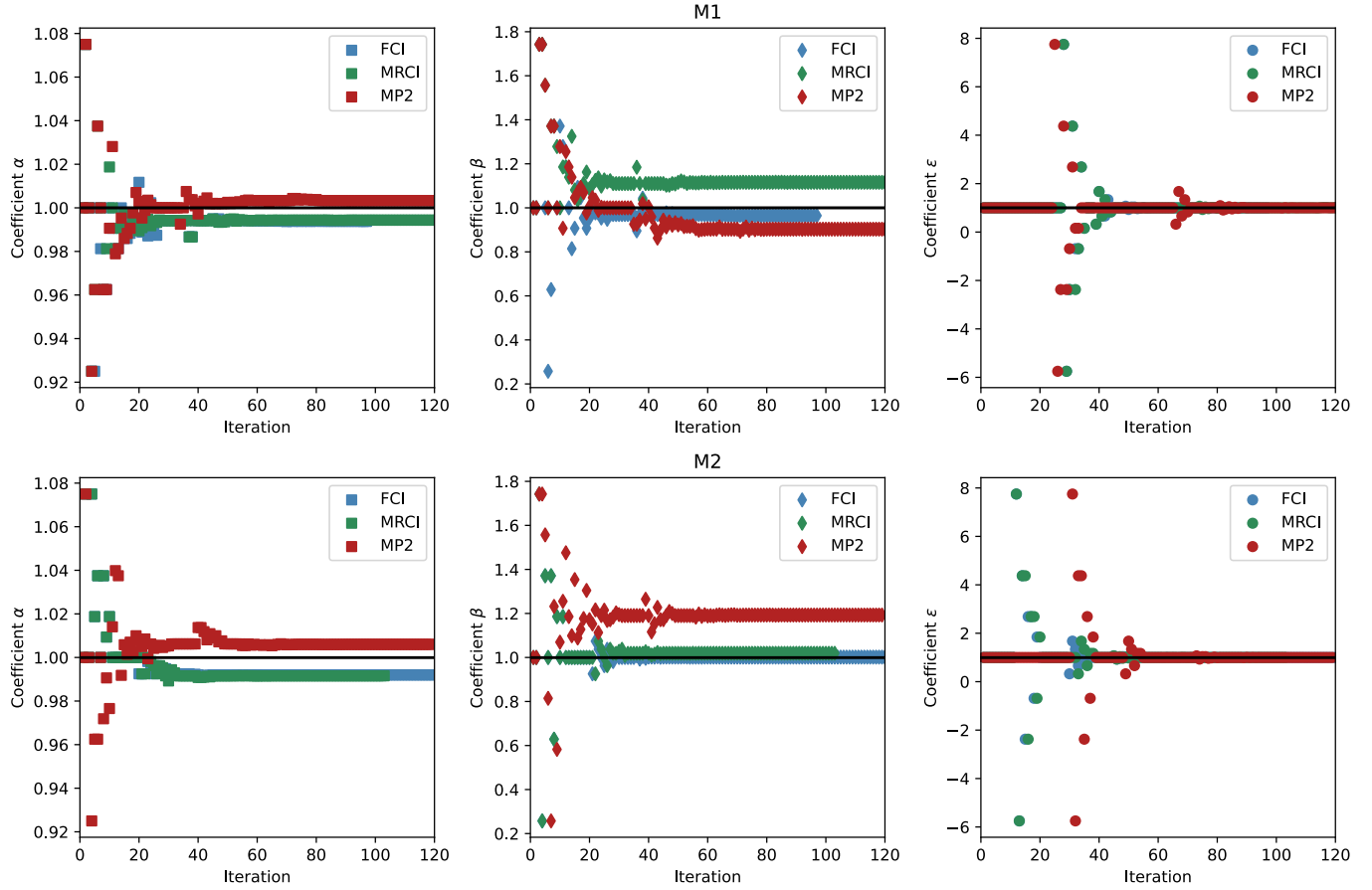


Figure S2: Parameter changes as a function of iteration for methods M1 (top) and M2 (bottom).

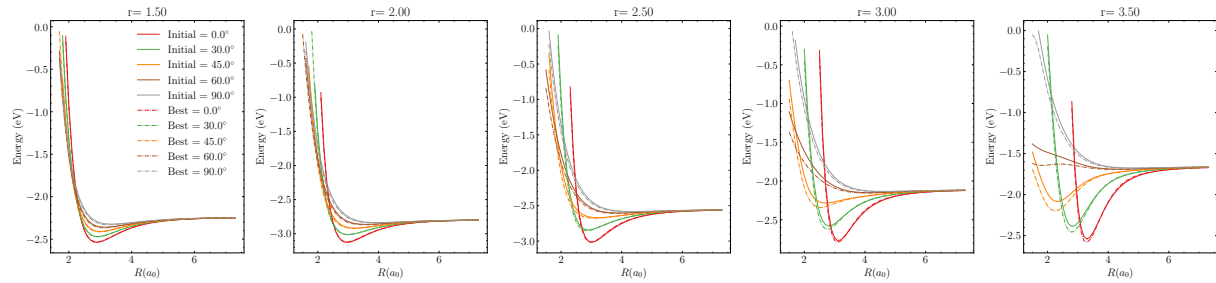


Figure S3: 1D cuts of the FCI PES obtained from the M1 procedure along R for fixed r_{HH} and different angles (θ).

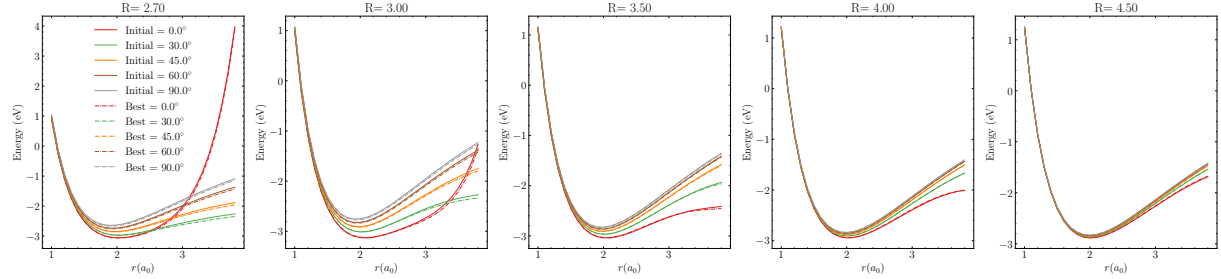


Figure S4: 1D cuts of the FCI PES obtained from the M1 procedure along r_{HH} for fixed R and different angles (θ).

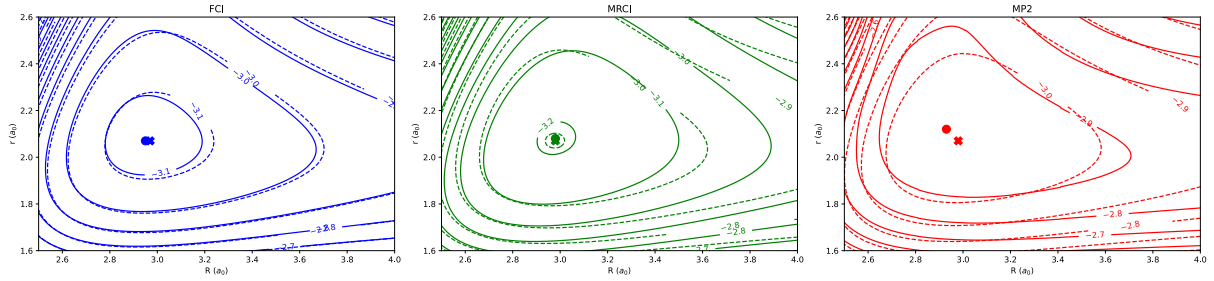


Figure S5: Potential energy surface 2D projection $V(R, r)$ at $\theta = 0^\circ$ obtained from the M1 procedure for the three potentials studied in this work. The dotted lines represent the unmorphed potential, complementary full lines show the morphed potential. Isocontours are separated by 0.1 eV. The minimum of the potential is indicated with a dot and a cross for the unmorphed and morphed potential.

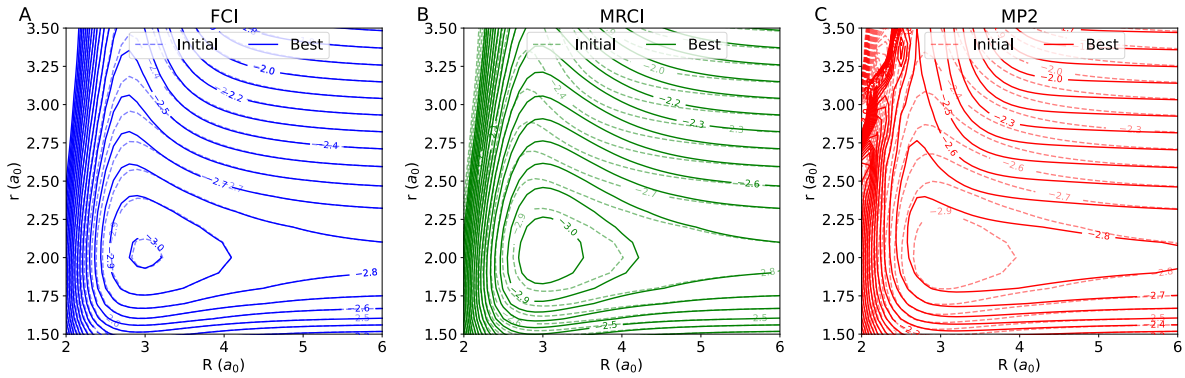


Figure S6: Potential energy surface 2D projection $V(R, r)$ at $\theta = 30^\circ$ obtained from the M1 procedure for the three potentials studied in this work. The dotted lines represent the unmorphed potential; complementary full lines show the morphed potential. Isocontours are separated by 0.1 eV.

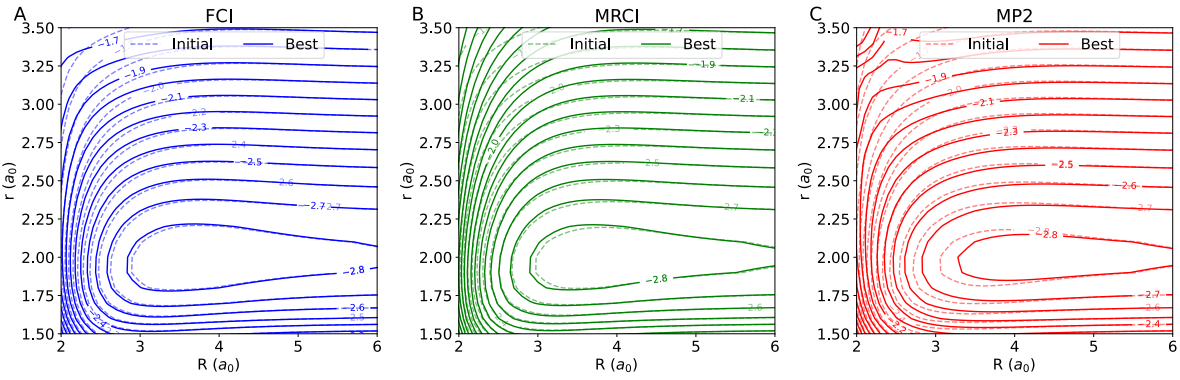


Figure S7: Potential energy surface 2D projection $V(R, r)$ at $\theta = 60^\circ$ obtained from the M1 procedure for the three potentials studied in this work. The dotted lines represent the unmorphed potential; complementary full lines show the morphed potential. Isocontours are separated by 0.1 eV.

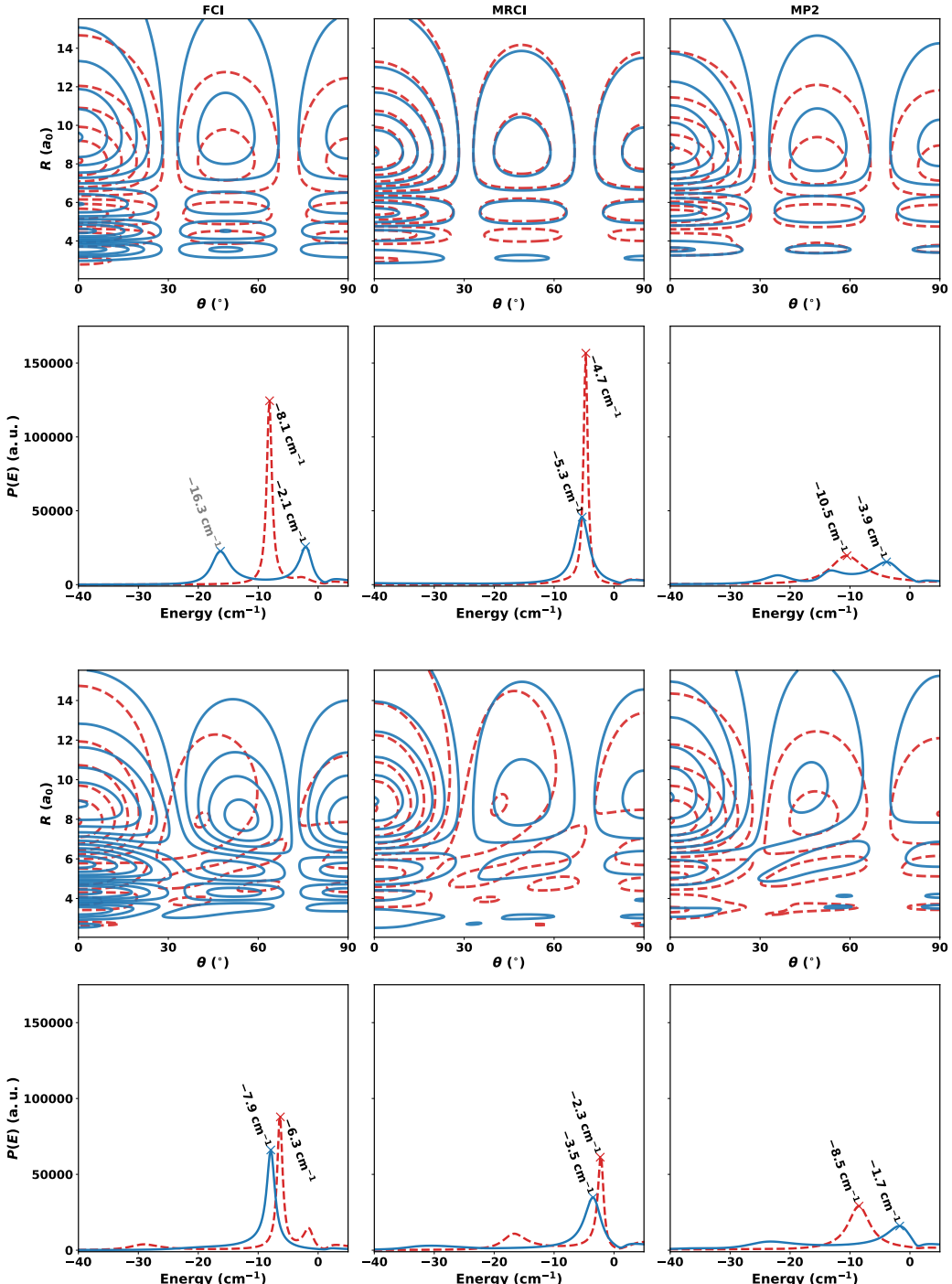


Figure S8: Comparison of the unmorphed (red, dotted) and morphed (blue) absolute value squared resonance wave functions in two dimensions (R, θ) in the case of para-H₂⁺ $\ell = 4, J = 4$ (upper two rows) and ortho-H₂⁺ $\ell = 4, J = 5$ (lower two rows) for resonance energies as marked and labelled in the corresponding cross sections are shown as a function of binding energy (second and fourth rows for para and ortho, respectively). The resonance wave functions have been scaled to have a maximal value of one, and the contours occur at 0.01, 0.1, 0.25, 0.5, 0.75 and 0.99.

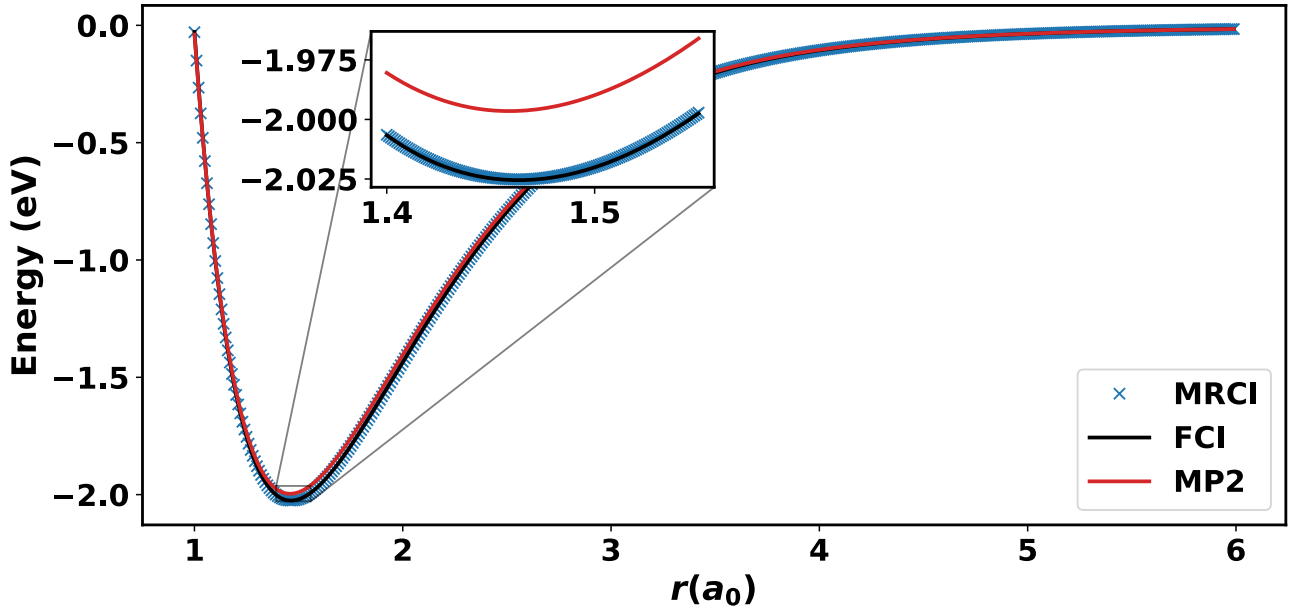


Figure S9: 2-body potential for the HeH^+ molecule. The inset shows the region close to the equilibrium geometry. Zero of energy is at the $\text{He}+\text{H}^+$ asymptote. For HeH^+ the experimentally determined (49) dissociation energy is $D_e = 16456.23 \text{ cm}^{-1}$ compares with 16406.04 (FCI), 16403.96 (MRCI+Q), and 16171.65 (MP2) cm^{-1} from the fitted 2-body potentials. The difference of 235 cm^{-1} between FCI and MP2 is substantial. Remaining differences between experiment and FCI are due to basis set incompleteness and non-Born-Oppenheimer effects, not included in the calculations. For other systems, such effects have been estimated at several ten up to 100 cm^{-1} on total energies. (50)

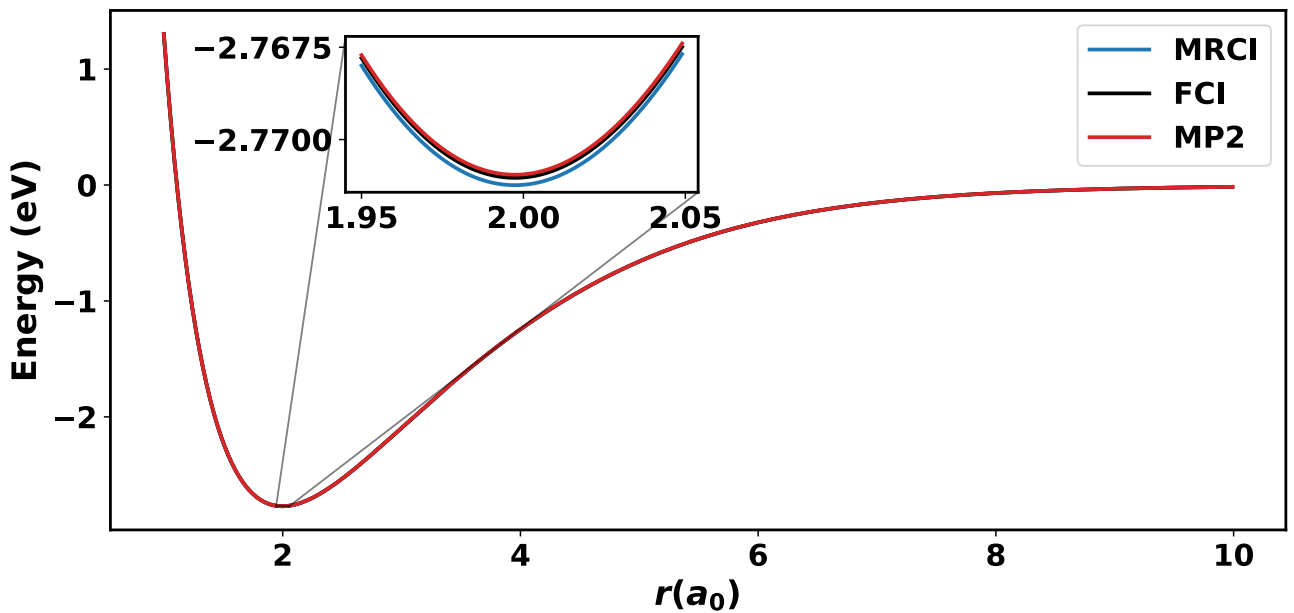


Figure S10: 2-body potential for the H_2^+ molecule. The zero of energy is the $\text{H}+\text{H}^+$ asymptote and the inset shows the region close to the equilibrium geometry. The experimentally determined (51) dissociation energy $D_0 = 21379.36 \pm 0.08 \text{ cm}^{-1}$ compares with 21428.5 (FCI), 21430.1 (MRCI+Q), and 21427.5 (MP2) cm^{-1} . The location of the ground states ($v = 0, j = 0$) was determined using the LEVEL code. (52) Remaining differences between experiment and FCI are due to basis set incompleteness and non-Born-Oppenheimer effects, not included in the calculations. For other systems, such effects have been estimated at several ten up to 100 cm^{-1} on total energies. (50)

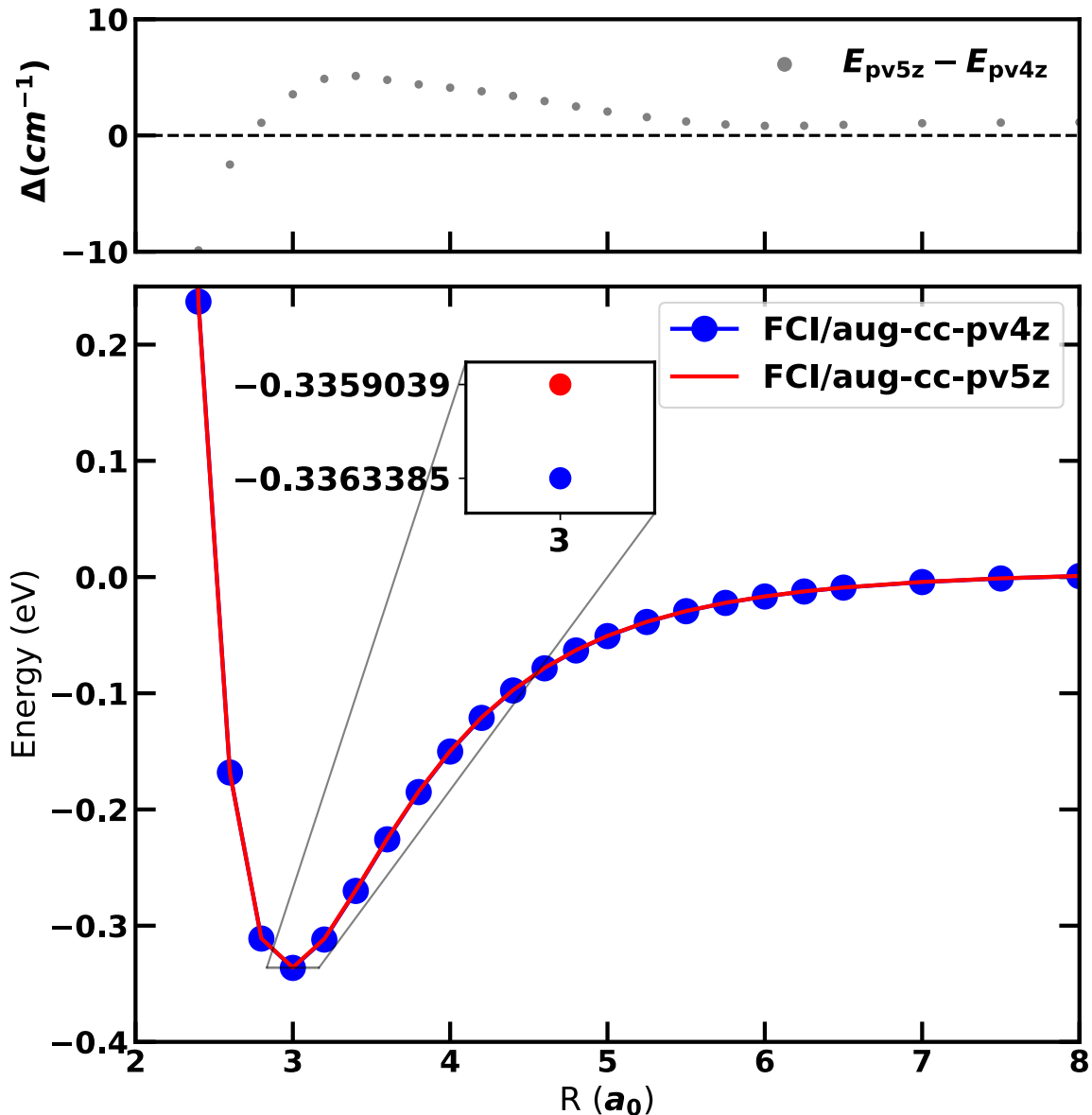


Figure S11: Interaction energy for $\text{He}-\text{H}_2^+$ along the R -coordinate for $r = r_{\text{eq}}$ and $\theta = 0$ from FCI calculations with the aug-cc-pv4z (blue) and aug-cc-pv5z (red) basis sets. The top panel shows the energy difference $\Delta = E_{\text{av5z}} - E_{\text{av4z}}$ in cm^{-1} when using the two basis sets. The inset shows the energy difference at the equilibrium position. The zero of energy of the system is the energy of the reactants He and H_2^+ .

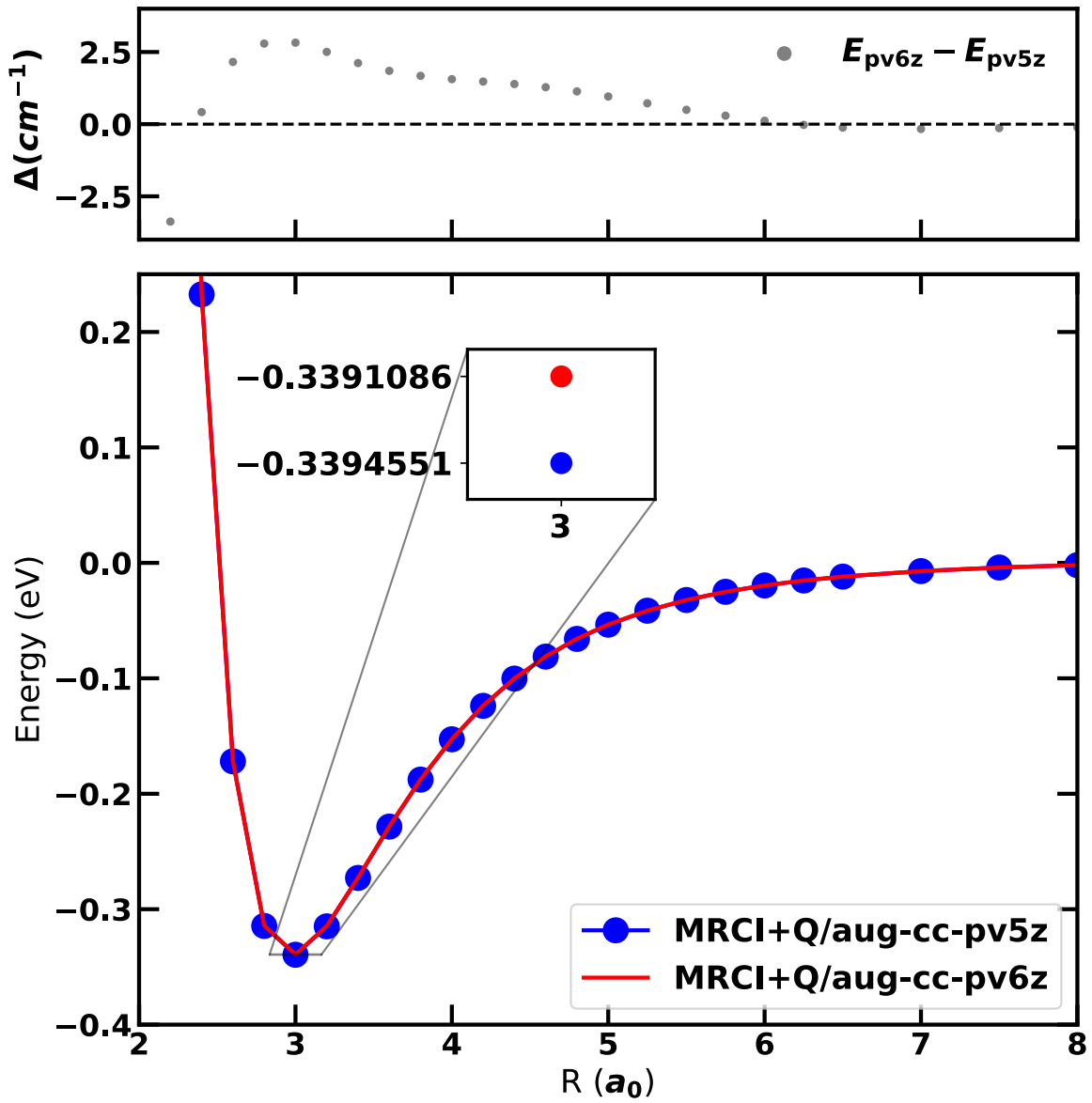


Figure S12: Interaction energy for $\text{He}-\text{H}_2^+$ along the R -coordinate for $r = r_{\text{eq}}$ and $\theta = 0$ from MRCI+Q calculations with the aug-cc-pv5z (blue) and aug-cc-pv6z (red) basis sets. The top panel shows the energy difference $\Delta = E_{\text{av6z}} - E_{\text{av5z}}$ in cm^{-1} when using the two basis sets. The inset shows the energy difference at the equilibrium position. The zero of energy of the system is the energy of the reactants He and H_2^+ .

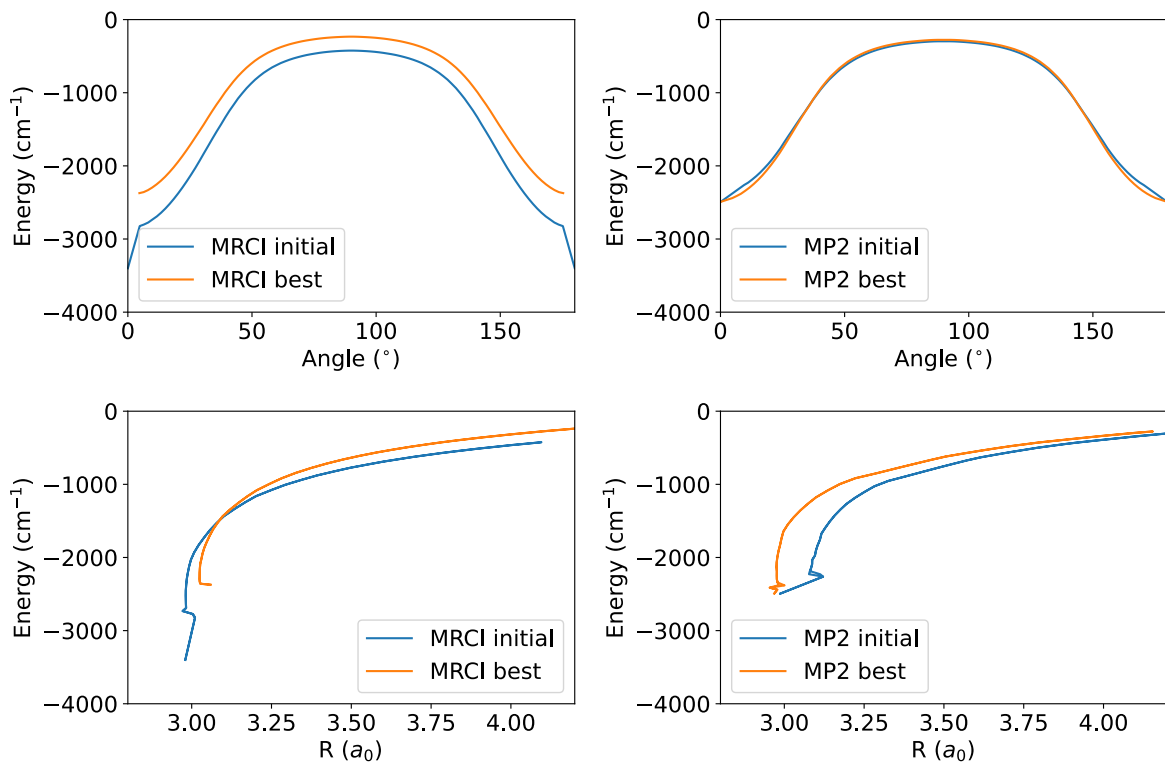


Figure S13: Minimum energy paths (MEPs) for the different surfaces obtained from the M2 method with respect to the variables θ and R . The zero of energy of the path is the energy of the separated monomers.

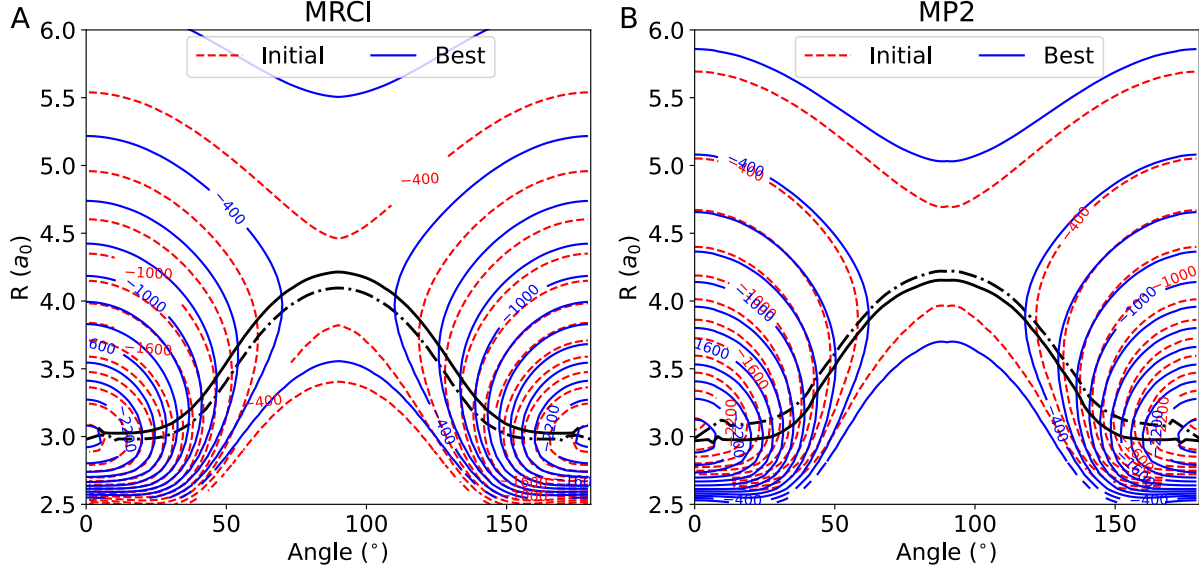


Figure S14: Minimum energy paths (MEPs) for the different surfaces studied before and after applying the morphing M2 method. In solid black, it is shown the MEP for the morph PES. In dotted black, the MEP is shown for the initial PES.

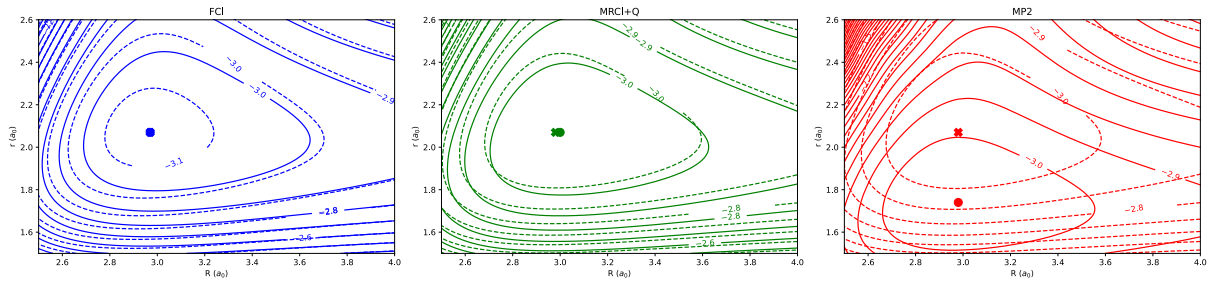


Figure S15: Potential energy surface 2D projection $V(R, r)$ at $\theta = 0^\circ$ obtained from the M2 procedure for the three potentials studied in this work. The dotted lines represent the unmorphed potential. Complementary full lines show the morphed potential. Isocontours are separated by 0.1 eV. The minimum of the potential is indicated with a dot and a cross for the unmorphed and morphed potential.

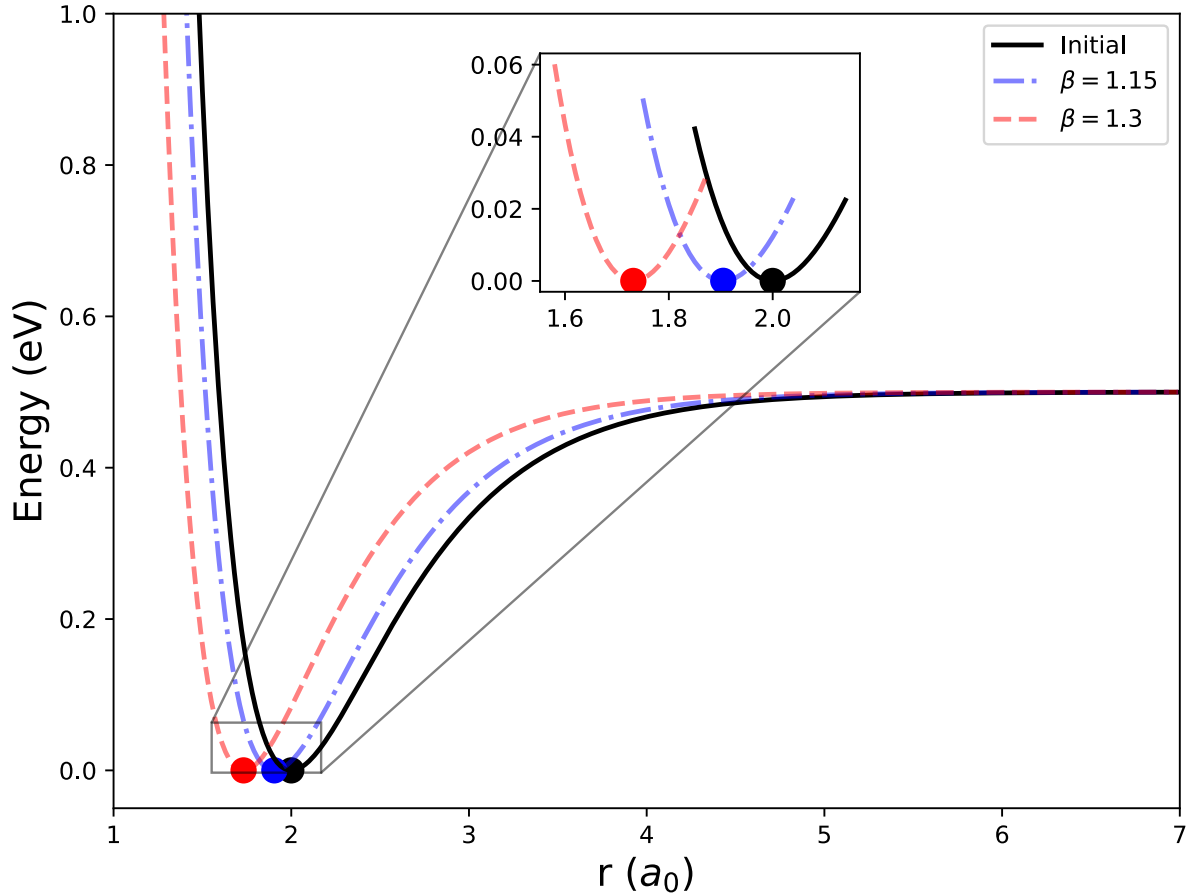


Figure S16: Schematic representation of the changes in the geometry by the morphing transformation for an example Morse potential curve. If the value of the scaling parameter $\beta > 1$, the equilibrium minima will be displaced to smaller values of coordinate r . The insight shows the change in the curvature close to the value of the equilibrium geometry

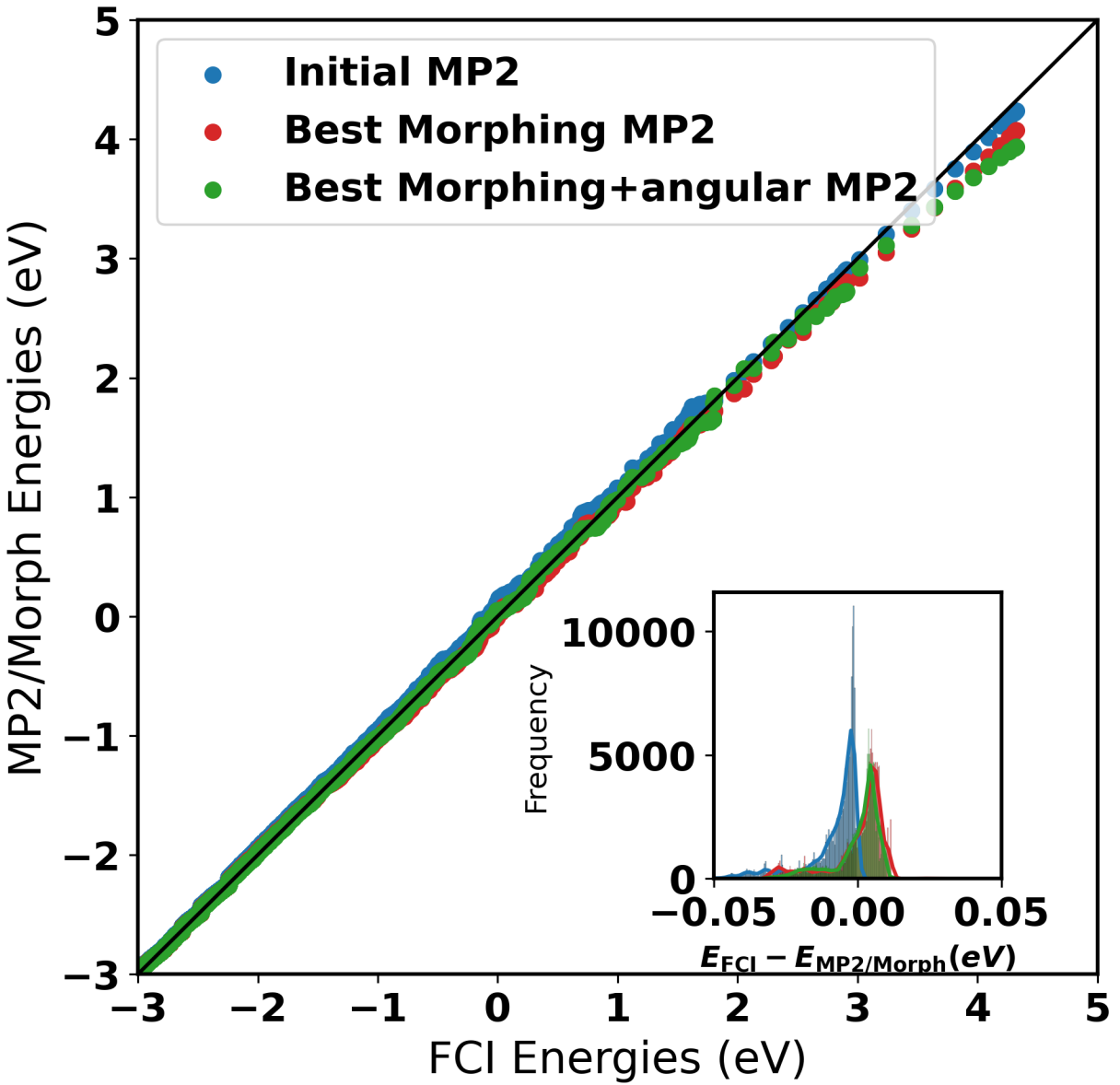


Figure S17: Scatter plot of the energies of the FCI surface vs the initial (blue) and morphed MP2 surface without (red) and with (green) angular morphing for the PES-to-PES procedure. In the inset of the figure, the distribution of differences $E_{\text{FCI}} - E_{\text{MP2}}$ for unmorphed and morphed MP2 surfaces, respectively. The Pearson correlation coefficients are 0.9984, 0.9988, and 0.9910 for unmorphed, morphed, and morphed+angular MP2 PESs and the RMSE decreases from 138 cm^{-1} to 88 cm^{-1} for morphing without angular correction and from 138 cm^{-1} to 75 cm^{-1} for morphing with angular correction for energies spanning $\sim 7 \text{ eV}$.

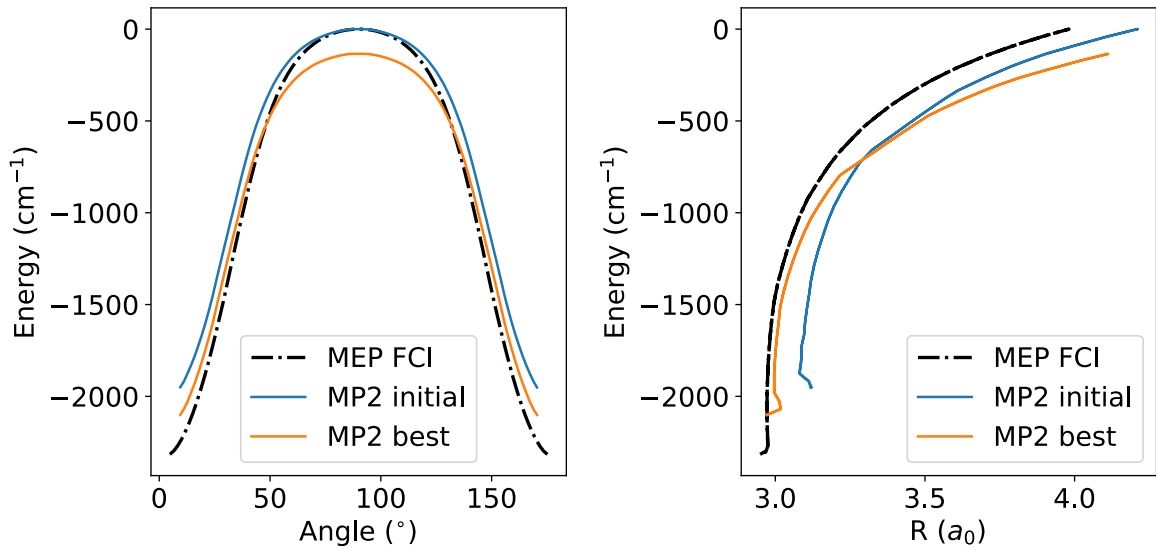


Figure S18: Minimum energy paths (MEPs) for the morph between the FCI and MP2 surface (PES to PES morphing) with respect to the variables θ and R . In black, the MEP for the FCI surface used as reference. The zero of energy of the path was chosen as the energy of the transition state for the unmorphed potential.

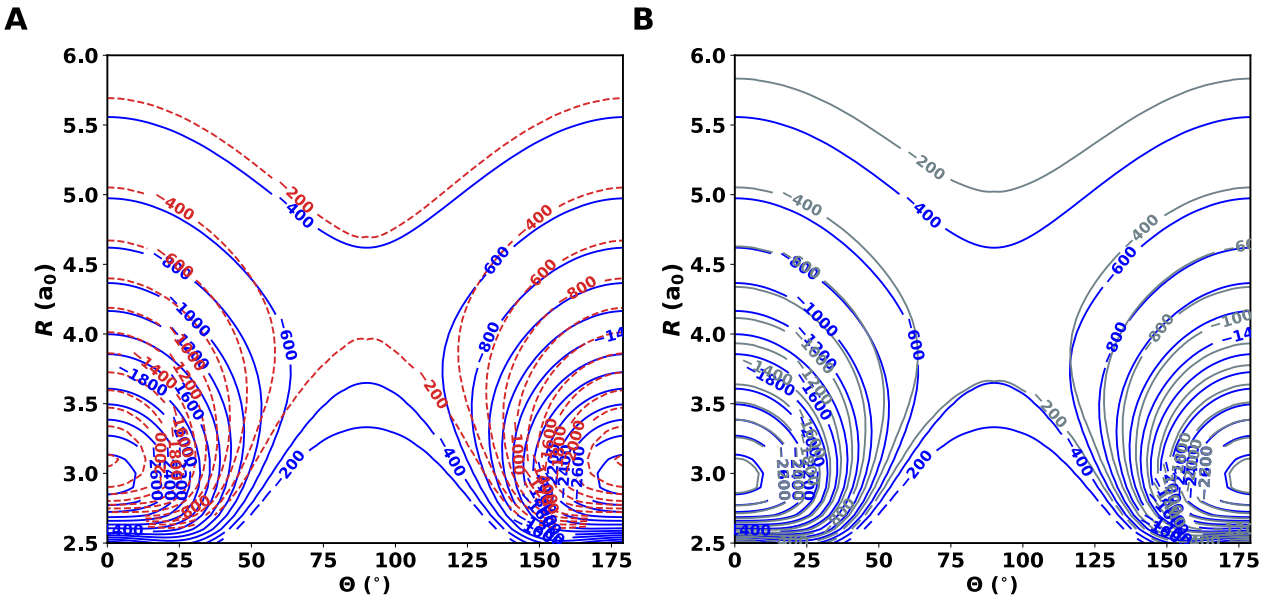


Figure S19: Morphing PES-to-PES + Angular correction. 2D projections of the PES for $r = 2.0 \text{ a}_0$. Panel A shows the unmorphed FCI (solid blue) compared with unmorphed MP2 (dashed light red). Panel B compares unmorphed FCI (solid blue) and best-morphed PES (grey). The zero of energy is set to the value of the PES at $r_{\text{HH}} = 2.0 \text{ a}_0$ and $R = \infty$. Energies are in cm^{-1} . Note that all data points are equally weighted; the performance of the morphing transformation may be changed by differentially weighting attractive and repulsive regions of the PES.

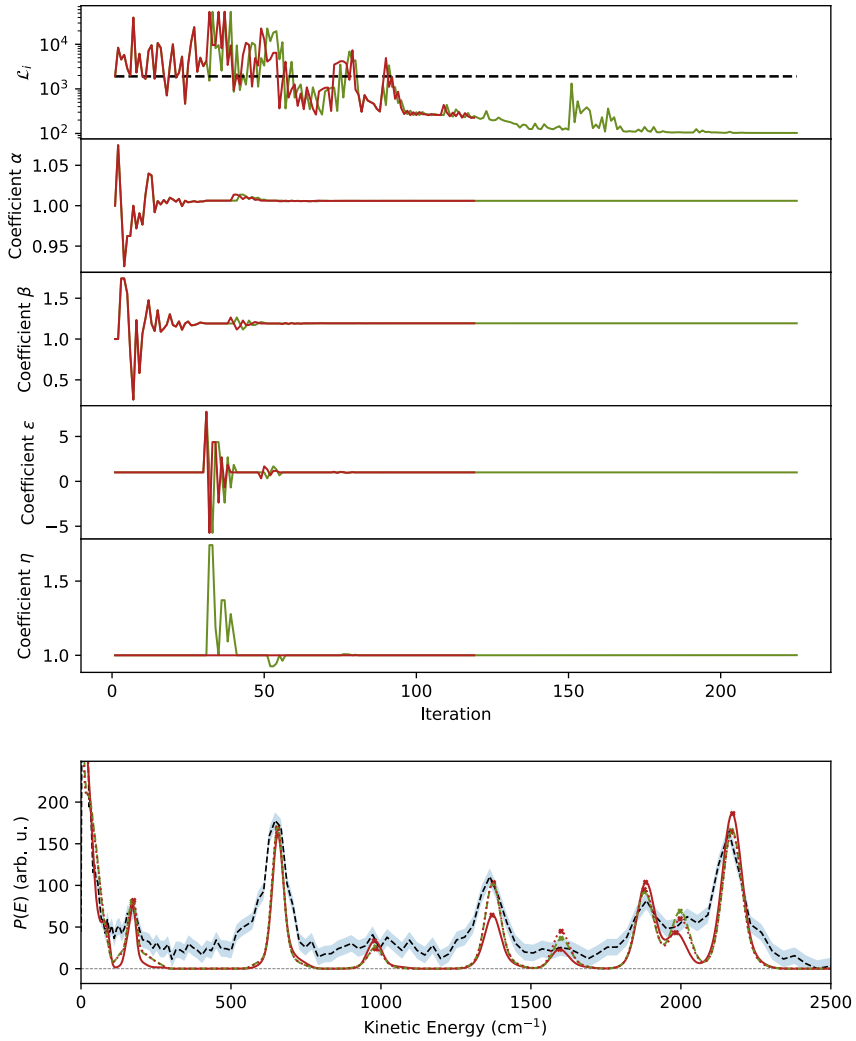


Figure S20: Overview for refinement of the MP2 PES including also angular morphing according to Eq. S1. The top five panels show (from top to bottom) the change in the loss function and the morphing parameters $\alpha, \beta, \varepsilon$ and η as a function of the optimisation iterations. Morphing without and with the angular degree of freedom are in red and green, respectively. The dashed black line in the top panel indicates the initial loss $\mathcal{L}_0 \approx 1900$ which compares final values of $\mathcal{L} \approx 225$ and $\mathcal{L} \approx 100$ without and with angular morphing, respectively. The bottom panel reports the cross sections from experiment (black line with regularization as the blue, shaded area), from the unmorphed MP2 PES (red, solid line), and the results from morphing without (red, dotted) and with (green, dashed) the angular degree of freedom.

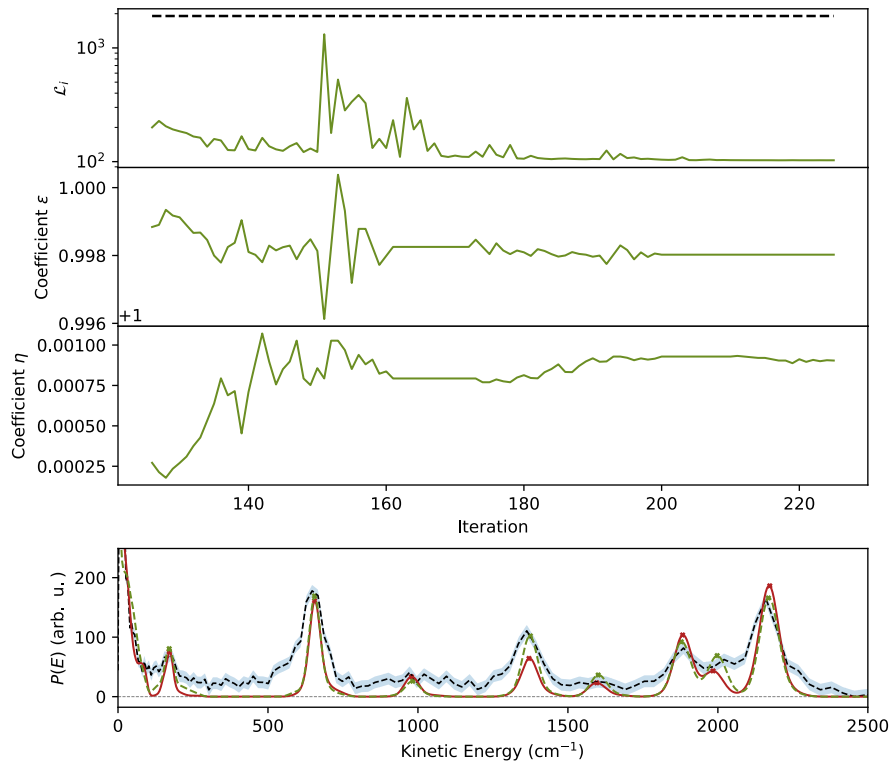


Figure S21: Similar to S20, details for refinement of the MP2 PES including also angular morphing according to Eq. S1. Only the last ~ 100 iterations and the morphing parameters ε and η are shown to better visualize the parameter variations.

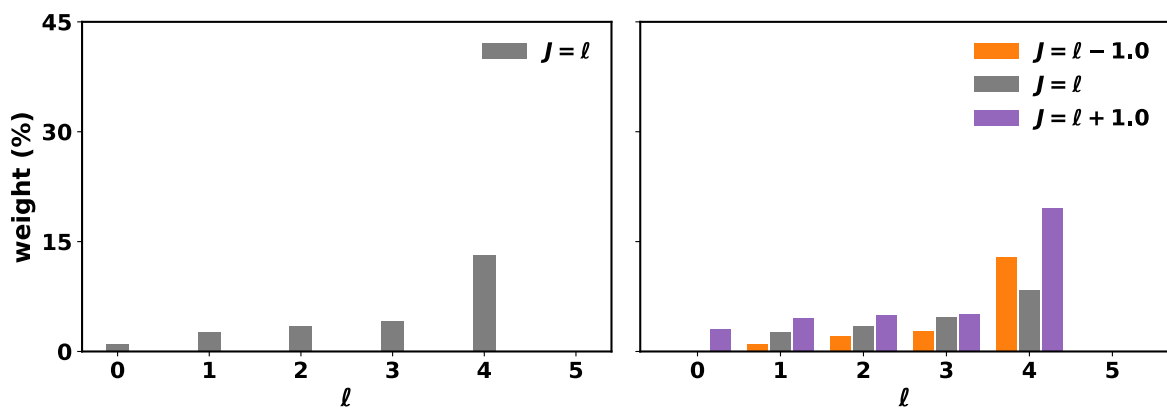


Figure S22: Relative contribution of each angular momentum state for collision of He(${}^3\text{P}$) with para- and ortho- H_2 (left and right panels, respectively) for the experimental collision energy $E_{\text{col}}/\text{k}_\text{B} \approx 2.5\text{K}$ and spread. Note that contributions for $\ell > 5$ are not shown since they are negligibly small.

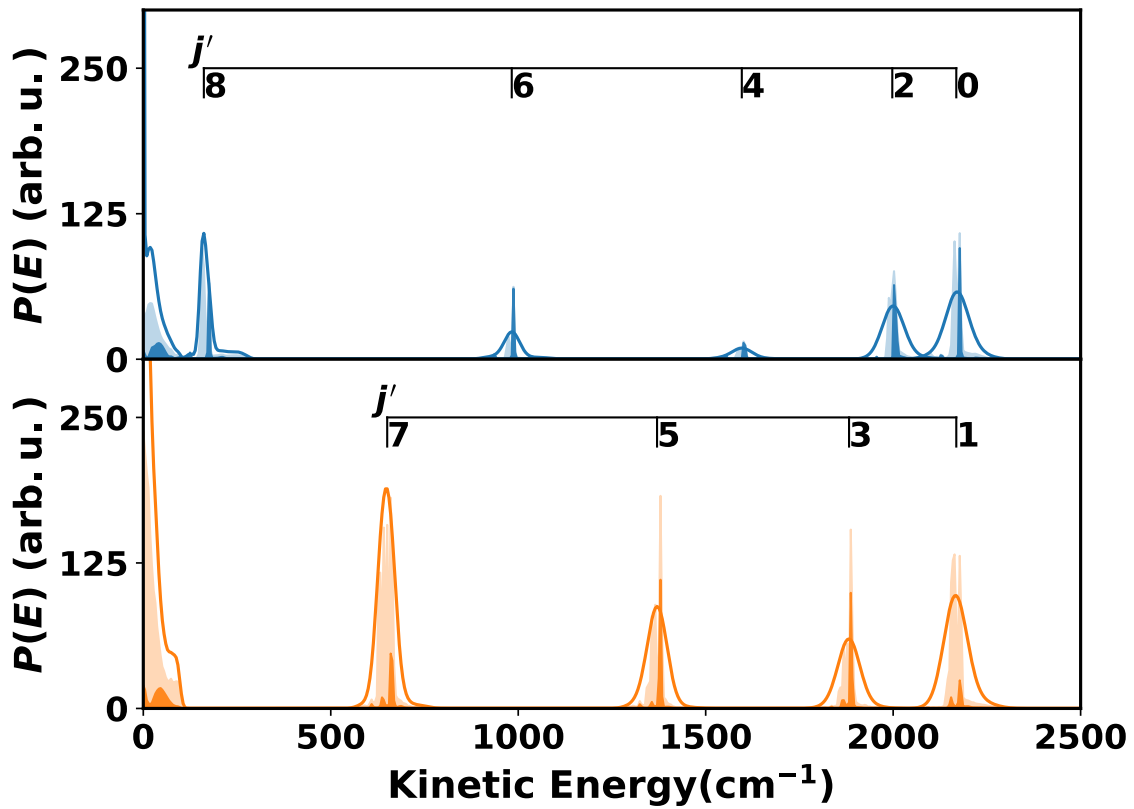


Figure S23: Theoretical kinetic energy histograms for para (above) and ortho (below) H_2^+ in their convoluted (line) and unconvoluted (shaded area) forms. The unconvoluted cross-sections have been scaled by a factor of 0.5 relative to the convoluted ones. The darkly shaded areas correspond to the dominant contributions to the cross-section ($\ell = 4, J = 4$ and $\ell = 4, J = 5$ for para and ortho respectively), whilst the lightly shaded areas include all initial ℓ and J contributions. The shown cross-sections were obtained using the unmorphed FCI potential.

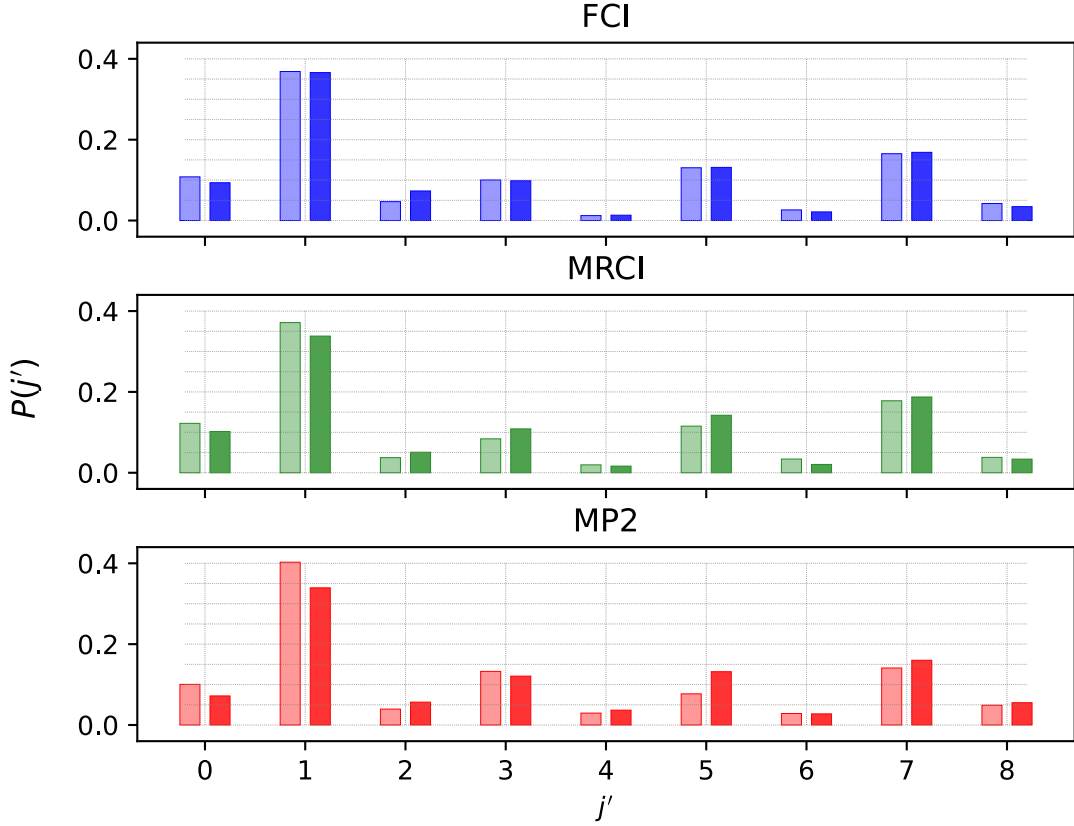


Figure S24: Final rotational state distributions $P(j')$ for the H_2^+ ion for the unmorphed (light colors) and morphed (dark colors) PESs using morphing M2. From top to bottom: FCI, MRCI, and MP2 PESs, respectively.

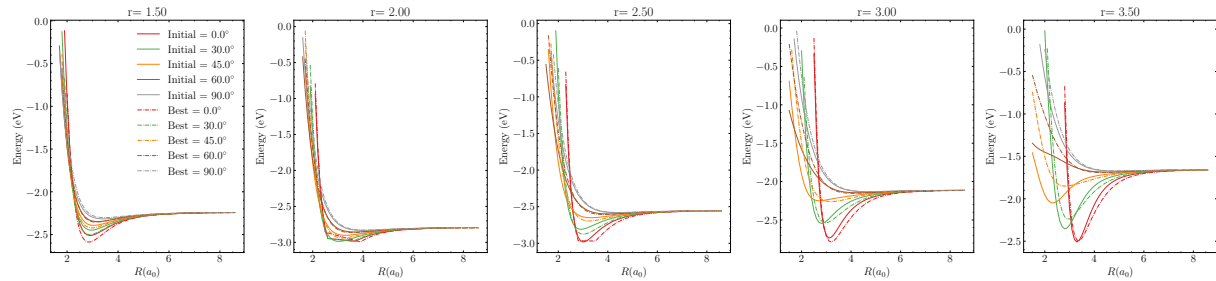


Figure S25: 1D cuts of the MRCI PES obtained from the M1 procedure along R for fixed r_{HH} and different angles (θ).

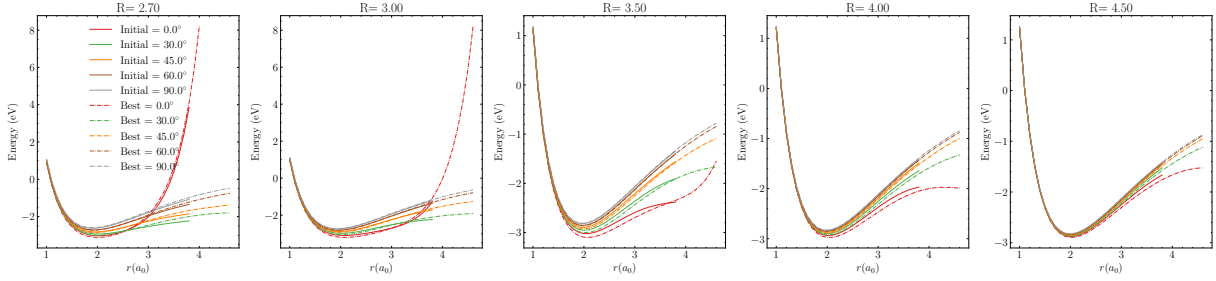


Figure S26: 1D cuts of the MRCI PES obtained from the M1 procedure along r_{HH} for fixed R and different angles (θ).

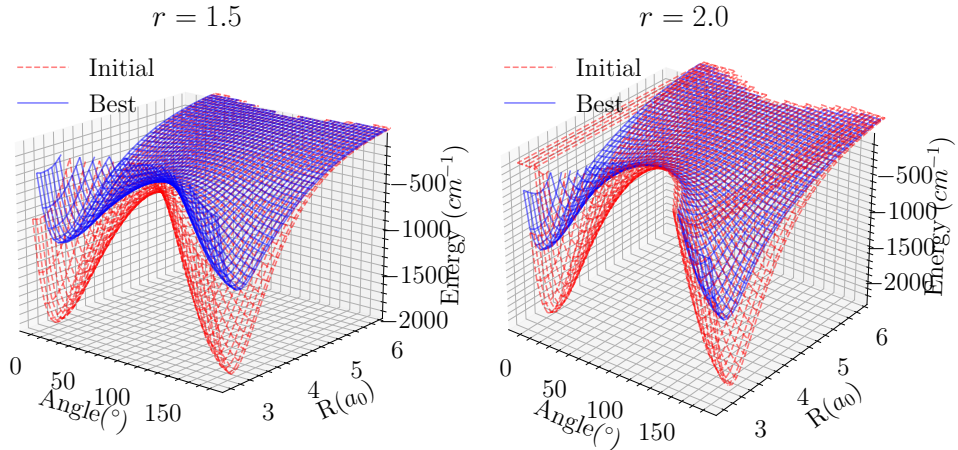


Figure S27: MP2 Potential energy surface from M1 procedure in 3D representation for fixed values of r_{HH} , on the top of the figure is indicated the value of r_{HH} . As zero of energy, it was considered the value at the given r_{HH} and $R = \infty$. Energies are in cm^{-1} and separated by 100 cm^{-1}

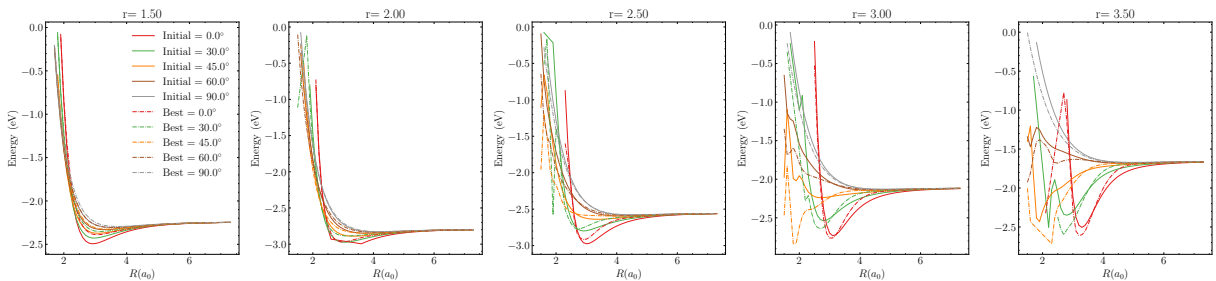


Figure S28: 1D cuts of the MP2 PES obtained from the M1 procedure along R for fixed r_{HH} and different angles (θ).

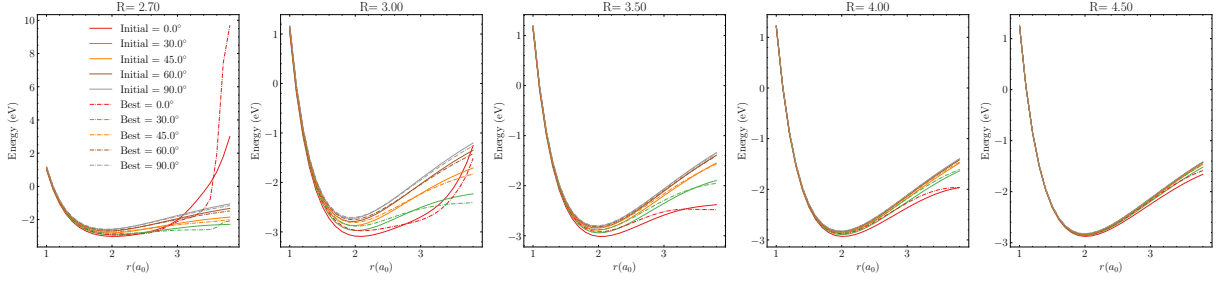


Figure S29: 1D cuts of the MP2 PES obtained from the M1 procedure along r_{HH} for fixed R and different angles (θ).

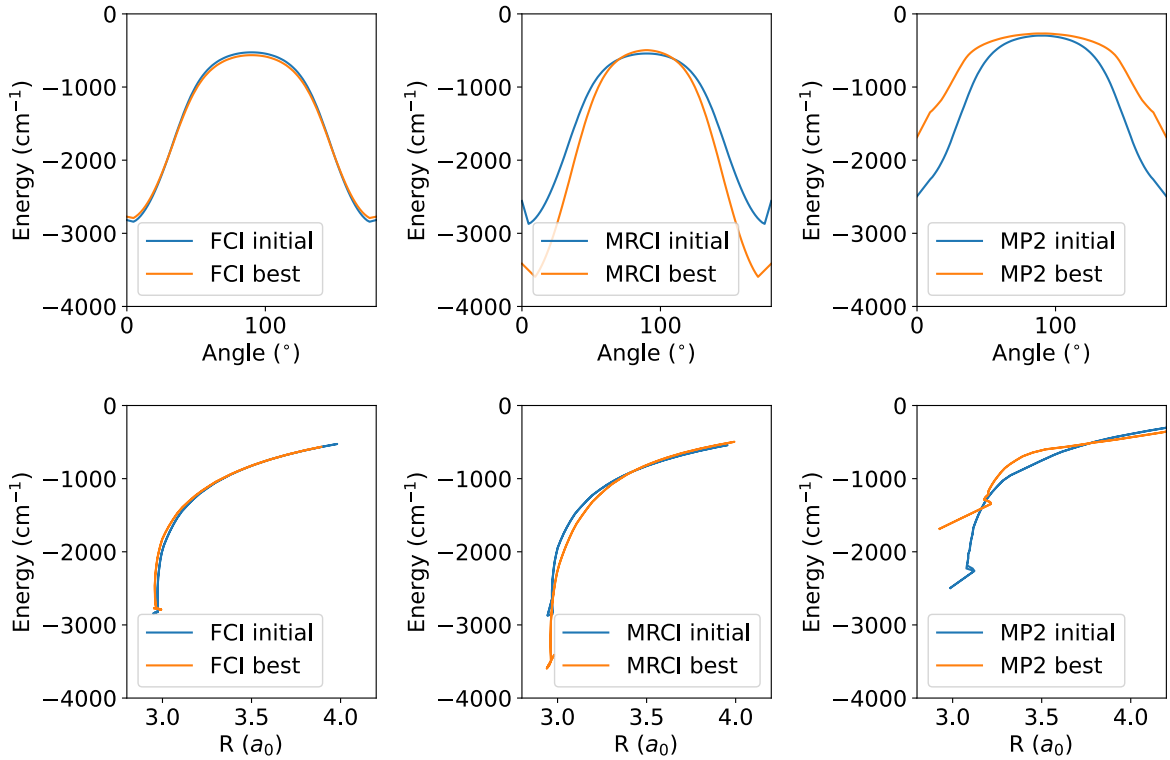


Figure S30: Minimum energy paths (MEPs) for the different surfaces obtained from the M1 method with respect to the variables θ and R . The zero of energy of the path is the energy of the separated monomers.

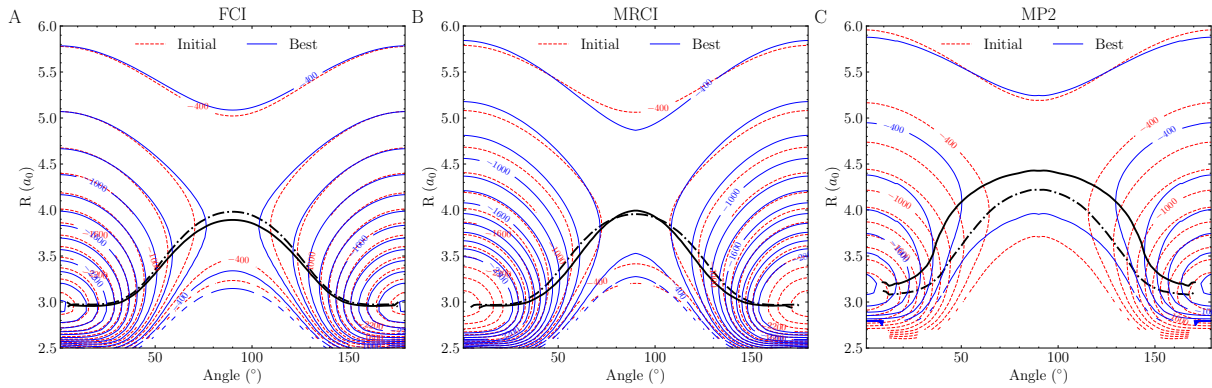


Figure S31: Minimum energy paths (MEPs) for the different surfaces studied before and after applying the morphing M1 method. In solid black, it is shown the MEP for the morph PES. In dotted black, the MEP is shown for the initial PES.

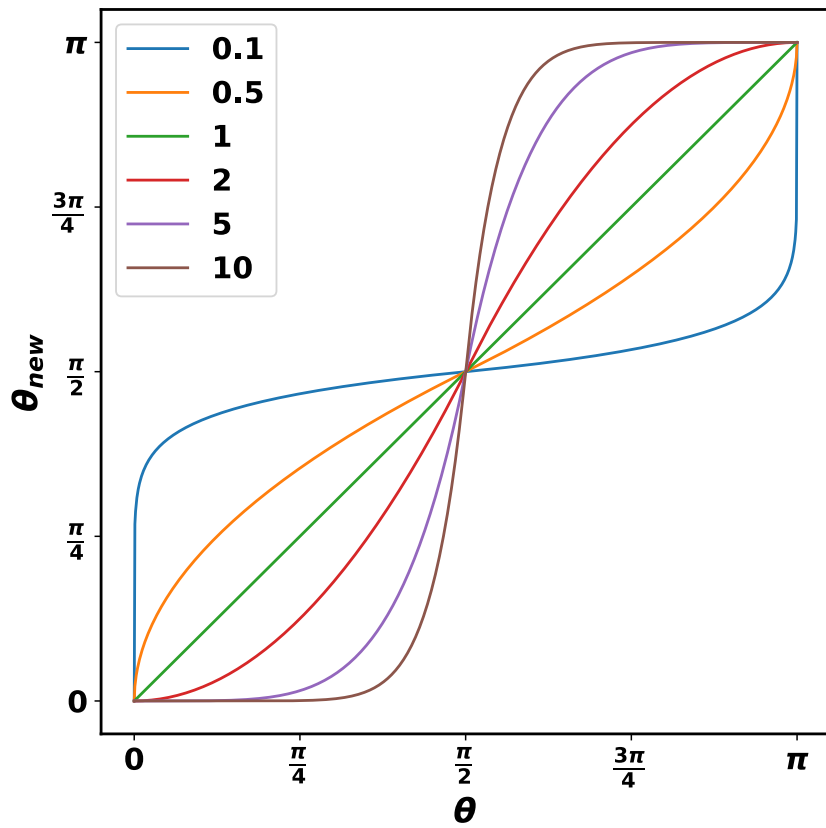


Figure S32: The angular power morphing function (see Eq. S1) used to transform the angular term of the PES. The transformation must keep the terms at $\theta = [0, \frac{\pi}{2}, \pi]$ invariant. The coloured lines corresponding to values of η ranging from 0.1 to 10 as indicated in the legend show the behaviour of the remapped angle as a function of the original in the domain $[0, \pi]$.